

# Shear wave attenuation and dispersion in melt-bearing olivine polycrystals:

## 1. Specimen fabrication and mechanical testing

Ian Jackson, Ulrich H. Faul, John D. Fitz Gerald, and Ben H. Tan

Research School of Earth Sciences, Australian National University, Canberra, Australia

Received 16 January 2003; revised 31 October 2003; accepted 7 January 2004; published 23 June 2004.

[1] Five melt-bearing polycrystalline olivine aggregates have been newly prepared by hot isostatic pressing and tested at high temperature and pressure with torsional forced-oscillation and microcreep methods. Cylindrical specimens, varying in average grain size from 7 to 52  $\mu\text{m}$ , were annealed and then tested during slow staged cooling under 200 MPa pressure from maximum temperatures of 1240–1300°C where they contained basaltic melt fractions ranging from  $\sim 0.0001$  to 0.037. For temperatures  $\geq 1000^\circ\text{C}$ , pronounced departures from elastic behavior are evident in strain energy dissipation  $Q^{-1}$  and associated dispersion of the shear modulus  $G$ . In marked contrast with the high-temperature viscoelastic behavior of melt-free materials, a broad dissipation peak is observed for each of the melt-bearing specimens - superimposed upon a melt-enhanced level of monotonically frequency- and temperature-dependent “background” dissipation. The oscillation period at which the peak is centered decreases systematically with increasing temperature. A “global” model comprising an Andrade-pseudoperiod background plus Gaussian peak accounts adequately for the variation of  $Q^{-1}$  with frequency, temperature, average grain size and melt fraction. In the following paper (Part II) a microstructural explanation for the observed viscoelastic behavior is sought and the global model is used to extrapolate the experimental data to the conditions of teleseismic wave propagation in the Earth’s upper mantle. **INDEX TERMS:** 3909 Mineral Physics: Elasticity and anelasticity; 5102 Physical Properties of Rocks: Acoustic properties; 5120 Physical Properties of Rocks: Plasticity, diffusion, and creep; 5144 Physical Properties of Rocks: Wave attenuation; **KEYWORDS:** anelasticity, viscoelasticity, seismic wave attenuation, olivine, partial melting, grain boundary sliding

**Citation:** Jackson, I., U. H. Faul, J. D. Fitz Gerald, and B. H. Tan (2004), Shear wave attenuation and dispersion in melt-bearing olivine polycrystals: 1. Specimen fabrication and mechanical testing, *J. Geophys. Res.*, *109*, B06201, doi:10.1029/2003JB002406.

### 1. Introduction

[2] Partial melting has often been invoked to explain regions of relatively low wave speeds and high attenuation in the Earth’s interior especially in the upper mantle [e.g., *Anderson and Sammis*, 1970; *Mavko and Nur*, 1975; *Shankland et al.*, 1981; *Forsyth*, 1992]. Given the paucity of directly relevant experimental observations, such analyses of seismological data have relied heavily upon the predictions of theoretical models [*Walsh*, 1968, 1969; *O’Connell and Budiansky*, 1977; *Mavko*, 1980; *Schmelting*, 1985; *Hammond and Humphreys*, 2000a, 2000b]. Such models quantify the dependence of seismic wave speeds and attenuation upon melt fraction and melt viscosity  $\eta$ , and importantly, upon the nature of the grain-scale melt distribution and the angular frequency  $\omega$  of the applied stress field.

[3] The model microstructure typically consists of fluid-filled inclusions of specified shape (e.g., ellipsoids, grain-boundary films, or grain-edge tubes) and connectivity embedded within a crystalline matrix, subject to an exter-

nally imposed stress field. As a consequence of the distortion of the matrix, each fluid inclusion is exposed to a particular state of tensorial stress. Depending upon the frequency of the applied stress, any one of four distinct fluid stress regimes may be encountered: glued, saturated-isolated, saturated-isobaric and drained, listed here in order of decreasing frequency [*O’Connell and Budiansky*, 1977]. At sufficiently high frequencies, within the glued regime, the fluid is able to support a non-hydrostatic stress with an effective shear modulus  $|G| = \omega\eta$  not substantially less than the matrix rigidity so that the relative tangential displacement of neighboring grains and hence the influence of the fluid are minimal. The saturated-isolated regime, where the fluid no longer supports shear stress but fluid pressure varies between (even adjacent) inclusions of different orientation, is encountered at somewhat lower frequencies. For still lower frequencies, fluid pressures are equilibrated by fluid flow between adjacent inclusions (“melt squirt,” [*Mavko and Nur*, 1975]) in the saturated-isobaric regime. Finally, at very low frequencies, drained conditions will apply for which no stress-induced perturbation of pore fluid pressure (relative to that in an external reservoir) can be sustained.

[4] The transition between the glued and saturated-isolated regimes, effected by local viscous relaxation in the melt, and the transition between the saturated-isolated and saturated-isobaric regimes associated with melt squirt are possible melt-related causes of dispersion and attenuation of seismic waves in the Earth's interior. The characteristic timescales or frequencies for these transitions and the associated attenuation and modulus dispersion will be addressed in detail in Part II.

[5] Until recently, the laboratory investigation of the viscoelastic behavior of partially molten rocks has lagged behind the development of the theoretical models. Considerable technical difficulties must be overcome especially if experiments are to be performed at seismic frequencies and under conditions of simultaneously high temperature and pressure. For this reason some of the early work was performed at MHz frequencies with ultrasonic techniques. Thus *Sato et al.* [1989] were able to show that both compressional wave speed  $V_P$  and associated dissipation  $Q_P^{-1}$  vary smoothly with homologous temperature across the solidus for a natural spinel peridotite – without any discontinuity attributable to the onset of melting.

[6] *Berckhemer et al.* [1982] and *Kampfmann and Berckhemer* [1985] used torsional forced oscillation techniques to study shear-mode dissipation and modulus dispersion at seismic frequencies, atmospheric pressure and trans-solidus temperatures for various rock types. The dissipation measured for each specimen was modelled as a combination of a background varying monotonically with frequency and temperature, a broad dissipation peak displaced to progressively higher frequencies with increasing temperature, and for the highest temperatures and frequencies  $>1$  Hz, an additional frequency-independent background component. Again, both the dissipation and shear modulus varied smoothly with temperature across the solidus.

[7] Recent seismic-frequency work on fine-grained synthetic olivine-dominated materials has substantially clarified the nature of sub-solidus viscoelastic relaxation [*Tan et al.*, 1997, 2001; *Gribb and Cooper*, 1998; *Jackson et al.*, 2002; *Cooper*, 2003]. These observations consistently demonstrate the existence of a broad absorption band, plausibly associated with grain-boundary sliding, within which the dissipation and dispersion vary smoothly and monotonically with both frequency and temperature. Intensive study of a suite of high-purity, fine-grained olivine polycrystals has refined our understanding of the progressive transition in melt-free material from elastic through mainly anelastic to dominantly viscous behavior with increasing temperature and oscillation period, and has also provided the first observational constraints on the grain-size sensitivity of the viscoelastic behavior [*Jackson et al.*, 2002]. Extrapolation of the mild measured grain-size dependence to mantle grain sizes suggests that much of the attenuation in the upper mantle might be attributable to grain-boundary sliding under sub-solidus conditions [*Jackson et al.*, 2002].

[8] However, locally, in tectonic settings such as mid-ocean ridges, back arc basins and mantle wedges above subduction zones, upper-mantle seismic wave speeds and attenuation must surely be affected by partial melting. In the laboratory, systematically higher attenuation and lower shear moduli result from the addition of 5 vol% of a highly potassic melt to a fine-grained reconstituted dunite without any

qualitative change of the absorption-band behavior [*Gribb and Cooper*, 2000]. In marked contrast, narrow dissipation peaks centered near 1180°C were seen in  $\sim 2$  Hz resonance experiments on olivine polycrystals containing basaltic melt fractions of 0.004 to 0.13 by *Xu et al.* [2004].

[9] In this manuscript we report seismic-frequency experimental data for shear modulus dispersion and attenuation for a new suite of melt-bearing fine-grained olivine aggregates. For each of these materials we find a broad melt-related dissipation peak superimposed upon a background that varies monotonically with frequency and temperature as for melt-free olivine polycrystals. In Part II we describe the microstructures of these melt-bearing materials, and present a microstructural interpretation of the macroscopic mechanical behavior and an extrapolation to the conditions of seismic wave propagation in the Earth's upper mantle.

## 2. Experimental Methods and Data Analysis

### 2.1. Specimen Fabrication

[10] Fine-grained Fo<sub>90</sub> olivine polycrystals were prepared by hot-isostatic pressing of powders of either natural (San Carlos, Arizona) or synthetic (sol-gel) origin [*Tan et al.*, 2001; *Jackson et al.*, 2002]. For all but two of the six melt-bearing specimens, basaltic melt glass was mixed into the precursor powder; in specimen 6366 the small melt fraction (0.004) is associated with impurities in this particular batch of San Carlos olivine. The very small melt fraction ( $\sim 0.0001$ ) newly recognized in specimen 6380 of *Jackson et al.* [2002], previously regarded as melt-free, has the same origin. The specimens range in mean grain size from 6.5 to 52.3  $\mu\text{m}$ , in bulk [H<sub>2</sub>O] measured by IR spectroscopy from  $<10$  to 80 wt ppm, and in melt fraction  $\varphi$  at the highest temperature encountered during hot-pressing and subsequent annealing and mechanical testing, from  $\sim 0.0001$  to 0.037 (Table 1). A detailed description of the microstructures of these materials examined both before and after mechanical testing, including grain-size distributions, grain-scale melt distribution and the impact of the crystallization of orthopyroxene, clinopyroxene and plagioclase during staged cooling is presented in Part II.

### 2.2. Mechanical Testing

[11] Cylindrical specimens typically of 11.50 mm diameter and 30 mm length were precision-ground from the hot-pressed polycrystals. The density of each specimen was determined by the Archimedeian method involving immersion in ethanol. The specimens were then heat-treated either at  $\sim 100^\circ\text{C}$  in air (specimens 6335, 6366 and 6384) or at  $1200^\circ\text{C}$  under controlled CO/CO<sub>2</sub> atmosphere (6380, 6409 and 6410) in order to remove adsorbed moisture. However, small bulk concentrations of water (up to 20 wt ppm, Table 1) survived even  $1200^\circ\text{C}$  firing – presumably chemically bound in the interstitial glass. For mechanical testing, each specimen was enclosed in metal foil of  $\sim 60$   $\mu\text{m}$  thickness (either 99.95% Fe (6335) or Fe<sub>70</sub>Ni<sub>30</sub>) in order to isolate it radially (two or three layers) from the mild-steel jacket and longitudinally (single layer of foil) from the alumina torsion rods [*Jackson*, 2000]. The torsional forced-oscillation/microcreep testing was performed at 200 MPa argon confining pressure within an internally heated gas-medium apparatus [*Jackson and Paterson*, 1993]. The

**Table 1.** Andrade-Gaussian-Pseudoperiod Fits to  $Q^{-1}$  Data for Individual Melt-Bearing Olivine Aggregates<sup>a</sup>

	Specimen			Dissipation Background						Peak			Misfit			
	$\rho$ , gm cm <sup>-3</sup>	$d$ , $\mu\text{m}$	$\phi$	[H <sub>2</sub> O], ppm	$E_B$ , kJ/mol	$J_U$ , 10 <sup>-1</sup> , GPa <sup>-1</sup>	$n$	$\beta$ , 10 <sup>-2</sup> , s <sup>-n</sup> GPa <sup>-1</sup>	$\eta$ , 10 <sup>6</sup> , GPa s	$E_p$ , kJ/mol	$B$	$\mu$	$\sigma$	$\chi^2$	$N$	$(\chi^2/N)^{1/2}$
6366(SC)	3.326(1)	52.3	0.004	80	350	(0.2) <sup>b</sup>	.347(13)	.112(9)	3.5(57)	650	.054(4)	4.57(25)	2.53(22)	65.0	51	1.13
Low <sup>c</sup>					550	(0.2)	.238(36)	.365(36)	(1.00)	870	.104(20)	4.07(54)	2.72(42)	7.29	28 <sup>d</sup>	0.51
6409(SC)	3.330(1)	29.3	0.013	20	580	(0.2)	.222(8)	.385(28)	1.00(10)	880	.107(6)	4.13(19)	2.80(19)	20.6	55	0.61
High <sup>c</sup>					630	(0.2)	.215(8)	(.385)	1.54(15)	760	.109(9)	3.76(40)	2.39(43)	2.50	31	0.28
Low <sup>c</sup>					480	(0.2)	.300(24)	.283(29)	(.226)	690	.115(13)	2.98(28)	2.16(21)	4.32	31	0.37
6384(SG)	3.303(1)	27.5	0.037	70	420	(0.2)	.313(11)	.240(23)	.226(21)	690	.122(6)	3.35(14)	2.39(14)	11.2	59	0.44
High <sup>c</sup>					370	(0.2)	.327(11)	(.24)	.151(15)	510	.127(11)	2.41(47)	2.22(43)	1.09	35	0.18
Low <sup>c</sup>					590	(0.2)	.277(22)	.326(46)	(.280)	780	.083(14)	2.83(49)	2.53(36)	8.06	31	0.51
6410(SG)	3.323(1)	11.3	0.015	20	570	(0.2)	.271(11)	.299(37)	.280(24)	760	.091(7)	3.15(24)	2.67(23)	13.4	55	0.49
High <sup>c</sup>					560	(0.2)	.268(16)	(.299)	.255(21)	750	.090(10)	3.09(93)	2.69(11)	4.48	31	0.38
6335(SC)	3.305(1)	8.9	0.021	10	610	(0.2)	.304(17)	.25(7)	(0.23)	660	.054(12)	2.69(66)	2.69(58)	9.0	28 <sup>e</sup>	0.57
6380(SC)	3.339(1)	6.5	0.0001	<10	510	(0.2)	.36(8)	.15(12)	.26(11)	670	.027(18)	1.7(12)	3.3(11)	7.0	41	0.41

<sup>a</sup>Equation (16) with  $T_r$ , 1100SC.<sup>b</sup> $J_U$  unconstrained by  $Q^{-1}$  data alone.<sup>c</sup>“Low” 1000–1150°C; “high” 1150°C–1300°C.<sup>d</sup>Eight, 15, and 100 s data at 1000°C excluded from fit.<sup>e</sup>Highest temperature (1250°C) data for the texturally immature specimen 6335 excluded.

loading of all interfaces within the specimen assembly by the confining pressure facilitates the gripping of the specimen in a way that minimizes the extraneous compliance that often complicates the interpretation of experiments performed at atmospheric pressure. Confining pressure also helps minimize thermal microcracking and thereby maintain a melt distribution controlled by surface tension.

[12] Each specimen was annealed at the highest temperature (typically the same as the hot-pressing temperature) for a total of 6–110 hr (inclusive of hot-pressing) during which the mechanical behavior was monitored for any temporal evolution of the kind reported by *Tan et al.* [2001], and subsequently cooled slowly ( $\sim 1^\circ\text{C}$  per minute) and mechanically tested in stages to room temperature. Routine mechanical testing involved the successive conduct of torsional forced-oscillation tests at each of a series of seven representative periods across the interval 1–100 s at a torque amplitude responsible for a maximum shear stress of  $\sim 0.2$  MPa corresponding, at the highest temperatures, to maximum shear strains of  $1\text{--}2 \times 10^{-5}$ . The forced-oscillation testing was occasionally extended to periods as great as 1020 s. Complementary torsional microcreep tests provide information concerning the extent to which the non-elastic strains are recoverable following removal of the applied torque, along with useful constraints on steady state viscosity. Tests at halved torque amplitude allowed us to address the issue of linearity of the stress-strain-strain rate behavior. Experimental details and the procedures employed in the analysis of the raw forced-oscillation and microcreep data have been described previously [Jackson, 2000].

[13] Examination of a vertical section through one of the specimens of this study (6409) revealed that the Ni-Fe foil between sample and alumina torsion rod at one end had inadvertently been dislodged during assembly so that approximately half of that end of the sample was in direct contact with the alumina. A layer of melt  $\sim 20$   $\mu\text{m}$  thick formed in this area. In order to assess its influence on the torsional compliance of the assembly, the effect of a hypothetical layer of melt 10  $\mu\text{m}$  thick but covering the whole of the sample cross-section was modelled. The result shows that for a melt viscosity of  $\sim 10$  Pa s

(corresponding to olivine tholeiite at 1200°C) the compliance of the jacketed specimen is increased by only  $\sim 0.1\%$ . The influence of any thin boundary layer, like that inadvertently created in specimen 6409, is therefore negligible.

## 2.3. Modeling the Dissipation Data

### 2.3.1. High-Temperature Dissipation Background: The Andrade Model

[14] The empirically successful Andrade creep function

$$J(t) = J_U + \beta t^n + t/\eta \quad (1)$$

in which the successive terms describe the elastic response and transient and steady state Newtonian creep, respectively, has been widely used to describe linear viscoelastic behavior. The associated dynamic compliance, which represents the response to a sinusoidally time-varying stress, has real and negative imaginary parts given by the following functions of angular frequency  $\omega = 2\pi/T_0$

$$J_1(\omega) = J_U + \beta\Gamma(1+n)\omega^{-n} \cos(n\pi/2) \quad (2a)$$

and

$$J_2(\omega) = \beta\Gamma(1+n)\omega^{-n} \sin(n\pi/2) + 1/\eta\omega \quad (2b)$$

where  $\Gamma(1+n)$  is the Gamma function [Findley et al., 1976].

[15] The dissipation background and shear modulus are then calculable as

$$Q_B^{-1} = J_2(\omega)/J_1(\omega) \quad (3)$$

and

$$G = [J_1^2(\omega) + J_2^2(\omega)]^{-1/2}. \quad (4)$$

This approach has previously been shown to provide an excellent internally consistent description of “high-temperature background” dissipation and modulus dispersion for individual specimens tested over a range of oscillation period at a specified temperature [Gribb and Cooper, 1998;

[Jackson, 2000] but is potentially more flexible as argued below.

### 2.3.2. High-Temperature Dissipation Background: The Andrade-Pseudoperiod Model

[16] For a single specimen tested over a range of temperatures  $T$  and oscillation periods  $T_o$ , we introduce the master variable

$$X_B = T_o \exp[(-E_B/R)(1/T - 1/T_r)] \quad (5)$$

to be substituted for period  $T_o$  in the Andrade expressions for  $J_1(\omega)$  and  $J_2(\omega)$  given above. The master variable  $X_B$  is a pseudoperiod in the sense that  $X_B = T_o$  for  $T = T_r$  but for higher (lower) temperatures,  $X_B$  is greater (less) than  $T_o$  in order to account for the expected temperature dependence of viscoelastic relaxation times. In equation (5)  $T_r$  is an arbitrarily chosen reference temperature within the range accessed experimentally and  $E_B$  is an activation energy. This new approach [see also Cooper, 2003, pp. 272–273] has been successfully tested on the dissipation data for the individual melt-free olivine polycrystals of our previous study [Jackson *et al.*, 2002]. The Andrade-pseudoperiod approach being advocated here has the advantage over the previously used power law dependence of  $Q^{-1}$  on pseudoperiod [Jackson *et al.*, 2002] of coping with the progressive transition from essentially anelastic to viscous behavior encountered at sufficiently high  $T$ , small grain size  $d$  and long period  $T_o$  – evident, for example, in the mildly non-linear trends for the highest temperatures and longest periods in Figure 1. Moreover, it has the potential to describe not only the dissipation but also the associated modulus dispersion in an internally consistent manner.

### 2.3.3. Melt-Related Dissipation Peak

[17] As will be seen in the next section, our data for melt-bearing olivine polycrystals invariably display a dissipation peak superimposed upon a high-temperature background with the usual monotonic frequency and temperature dependence. The logical first choice for fitting the  $Q^{-1}$  peak is the Debye peak associated with the unique thermally activated anelastic relaxation time  $\tau = \tau_o \exp(E/RT)$  for the standard anelastic solid, for which

$$Q^{-1}(\omega\tau) = \Delta\omega\tau / (1 + \Delta + \omega^2\tau^2) \quad (6)$$

where  $\Delta$  is the relaxation strength [Nowick and Berry, 1972]. The full width at half height of the Debye peak is fixed at

$$\delta \log_{10} T_o|_T = \delta \log_{10} (\omega\tau) = 2 \log_{10} (2 + \sqrt{3}) = 1.14 \quad (7)$$

However, the dissipation peaks observed for the melt-bearing specimens of this study are consistently 2–3 times as wide in  $\log T_o$  (see below) – indicating that a broader distribution of anelastic relaxation times  $\tau$  is required. Instead of seeking to specify the underlying distribution  $D(\tau)$ , which remains an important longer-term goal, we have chosen here to model the dissipation peak by the following Gaussian function

$$Q_p^{-1} = B \exp(-z^2/2) \quad (8)$$

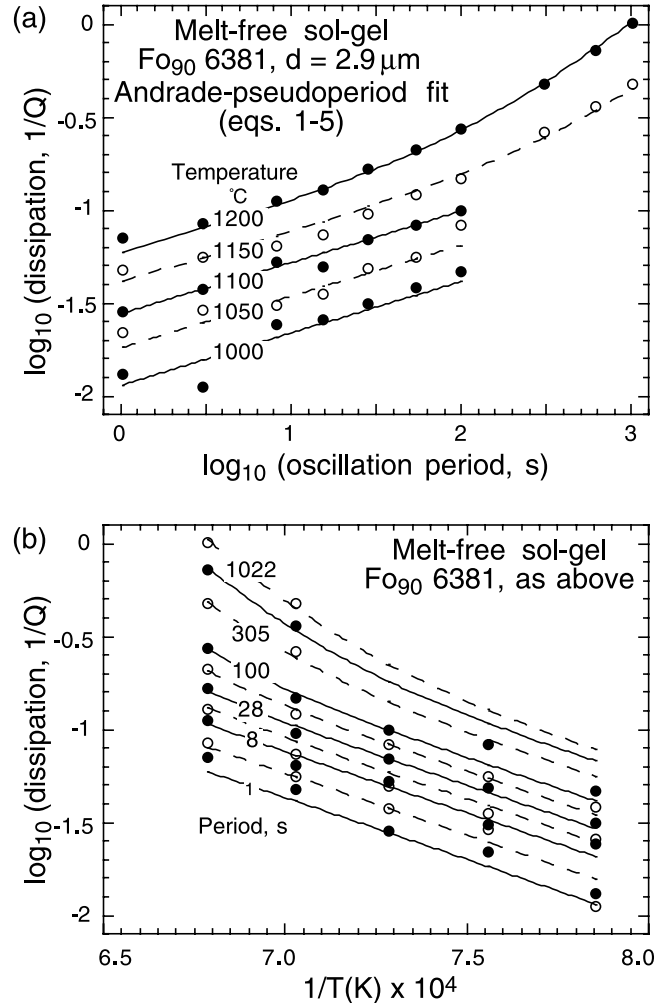


**Figure 1.** Representative dissipation data from torsional forced-oscillation tests on a melt-free  $Fo_{90}$  olivine specimen [Jackson *et al.*, 2002] highlighting the smooth monotonic variation of  $Q^{-1}$  with (a) period and (b) reciprocal temperature – very different from the behavior of the melt-bearing materials of the present study (Figures 2–7). See color version of this figure in the HTML.

with

$$z = (\ln X_p - \mu) / \sigma. \quad (9)$$

$B$  is the height of the dissipation peak and the physical significance of the parameters  $\mu$  and  $\sigma$  related respectively to peak position and width, is explained below. By analogy with equation (5) above, a pseudoperiod  $X_p$  for use in describing the dissipation peak is defined as

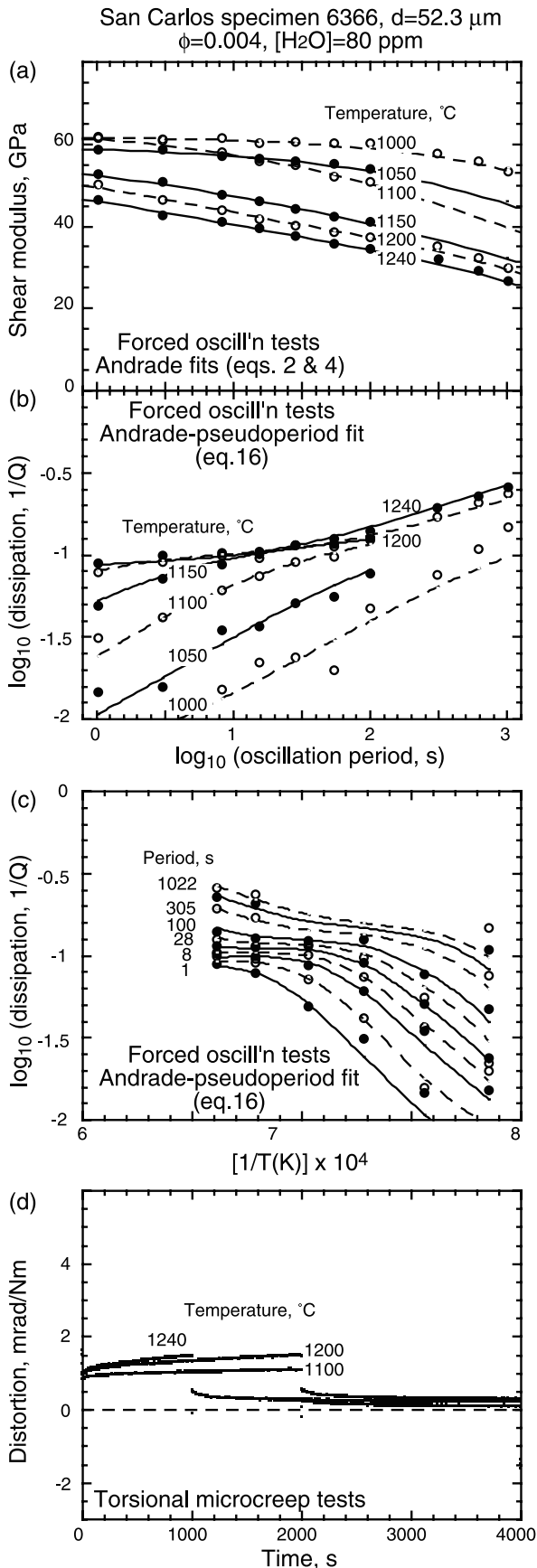
$$X_p = T_o \exp[(-E_p/R)(1/T - 1/T_r)] \quad (10)$$

with  $T_o$  in seconds. It follows from equations (8) and (9) that the locus of the center of the dissipation peak in  $(T_o, T)$  space is given by

$$\ln X_p - \mu = 0 \quad (11)$$

which, with  $X_p$  from equation (10), becomes

$$\ln T_{oP} = (E_p/R)(1/T_p - 1/T_r) + \mu. \quad (12)$$



$\mu$  is thus identified as the value of  $\ln X_p$  at the peak center - realized for peak-specific combinations of  $T_p$  and  $T_{oP}$  prescribed by equation (12);  $\sigma$  is a measure of peak width as follows. The values of  $T_o$  for which  $Q_p^{-1} = B/2$  are given by

$$\ln T_o = (E_p/R)(1/T - 1/T_r) + \mu \pm \sigma(2 \ln 2)^{1/2} \quad (13)$$

implying a full width at half height (in period) of

$$\delta \log_{10} T_o|_T = [2(2 \ln 2)^{1/2} / \ln 10] \sigma = 1.02 \sigma. \quad (14)$$

The full width at half height in reciprocal temperature at constant oscillation period is similarly derived from equation (13):

$$\delta(1/T)|_{T_o} = [2(2 \ln 2)^{1/2} R/E_p] \sigma = 2.35(R/E_p) \sigma. \quad (15)$$

It will be demonstrated below that the  $Q^{-1}(T_o, T)$  data for each of the melt-bearing specimens are very well described by a model of the form

$$Q^{-1} = Q_B^{-1} + Q_P^{-1} \quad (16)$$

with  $Q_B^{-1}$  and  $Q_P^{-1}$  given by equations (3) and (8), respectively.

#### 2.4. Temperature and Grain-Size Sensitivity of Viscosity

[18] For melt-free materials the viscosity  $\eta_{mf}$ , governing the contribution of steady state diffusional creep to the creep function (e.g., equation (1)), is expected to vary with temperature and grain size as

$$\eta_{mf} = \eta_0 d^p \exp(E/RT) \quad (17)$$

with  $p$  assuming the values of 2 and 3 for lattice diffusion and grain-boundary diffusion respectively and  $E$  being the activation energy for steady state diffusional creep [e.g., *Frost and Ashby*, 1982]. The influence of a small basaltic

**Figure 2.** Results of mechanical testing of specimen 6366. (a) Shear modulus versus log oscillation period at each of a series of temperatures. Forced-oscillation data are indicated by plotting symbols; curves represent the optimal Andrade fits (equation (4) with (2)). (b) Log dissipation measured in forced-oscillation tests versus log period at each of a series of temperatures. Data are indicated by the plotting symbols; curves represent the  $Q^{-1}(T_o, T)$  fit for this specimen (equation (16) along with (3), (2), (5) and (8–10)). (c) Same data and fit as in (b) but now plotted as log dissipation versus reciprocal absolute temperature at each of a series of oscillation periods (1, 3, 8, 15, 28, 54, 100, 305, 612, and 1022 s). (d) Microcreep records plotted as angular distortion versus time. The interval during which the steady torque is applied is terminated after either 1000 or 2000 s allowing observation of the partial recovery of the creep strain. See color version of this figure in the HTML.

melt fraction ( $\varphi < 0.05$ ), as documented by *Hirth and Kohlstedt* [1995], is to reduce the viscosity to

$$\eta_{mb} \approx \eta_{mf}/(1 + 50\varphi). \quad (18)$$

### 3. Results of the Mechanical Testing

#### 3.1. Generalities

[19] A striking characteristic of our results for melt-free materials is a simple monotonic variation of  $Q^{-1}$  with oscillation period and temperature represented by sub-parallel  $\log Q^{-1} - \log T_0$  trends for different temperatures [*Jackson et al.*, 2002] illustrated in Figure 1a. The smooth monotonic variation of  $Q^{-1}$  with period and temperature is equally evident in Figure 1b where the same data are plotted against  $1/T$  for each of series of fixed oscillation periods.

[20] As for the melt-free specimens tested by *Tan et al.* [2001] and *Jackson et al.* [2002], the behavior of the melt-bearing materials is essentially elastic for temperatures  $\leq 900^\circ\text{C}$ , but at higher temperatures appreciable dissipation and modulus dispersion (frequency or period dependence) are observed. In this latter regime, the frequency-dependent shear modulus  $G$  and strain energy dissipation  $Q^{-1}$ , and the creep rate evident in the records from the torsional micro-creep tests all vary systematically with temperature for each of the six melt-bearing specimens (Figures 2–7). However, Figures 2b–6b reveal a qualitatively different behavior for the melt-bearing materials of this study. Here, the dissipation is almost frequency-independent for periods of 1–100 s at temperatures of 1150–1200°C, but is more strongly frequency-dependent at both lower and higher temperatures and at longer periods. A qualitatively similar but more subtle variation with temperature of the strength of the frequency dependence of  $Q^{-1}$  is evident in Figure 7b for specimen 6380 with the smallest melt fraction.

[21] From Figures 2c to 7c where the same dissipation data are plotted against reciprocal absolute temperature for each of a series of oscillation periods, it is evident that the more complex variation of  $Q^{-1}$  with oscillation period and temperature in the melt-bearing specimens is associated with a dissipation peak superimposed on a monotonic high-temperature background reminiscent of that for the melt-free materials (Figure 1a). The dissipation peak moves systematically across the 1–1000 s observational window from long to short periods with increasing temperature. Use of the simple Andrade model (equations (2–4)) provides adequate fits to the modulus dispersion for each of the specimens at any given temperature (Figures 2a–7a) but unsurprisingly fails to cope with the complex frequency dependence of the dissipation for the melt-bearing specimens of the present study.

#### 3.2. The Temperature Dependence of the Shear Modulus

[22] For  $T \leq 900^\circ\text{C}$ , the behavior is essentially elastic with a temperature-dependent modulus at the representative oscillation period of 8 s in close accord with expectations based on high-frequency single-crystal elasticity data (Figure 8a). At higher temperatures the intense strain energy dissipation measured for the melt-bearing specimens of the present study is accompanied by pronounced modulus

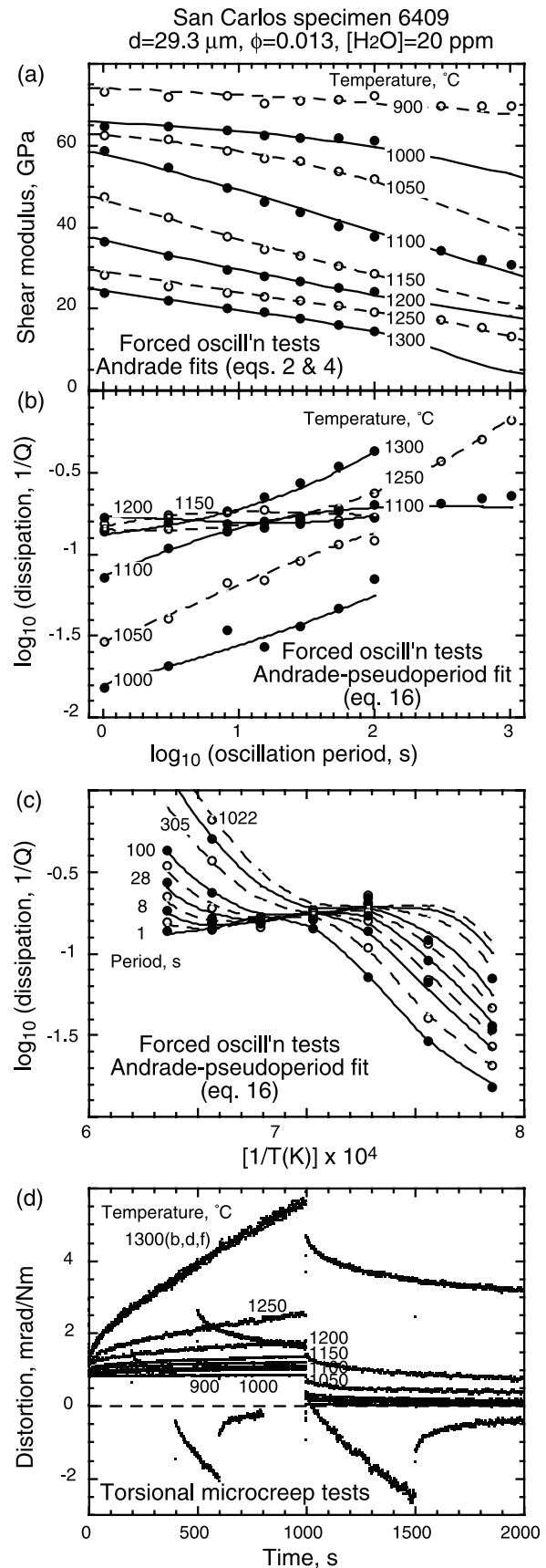


**Figure 3.** Results of mechanical testing of specimen 6409. Details as for Figure 2. See color version of this figure in the HTML.

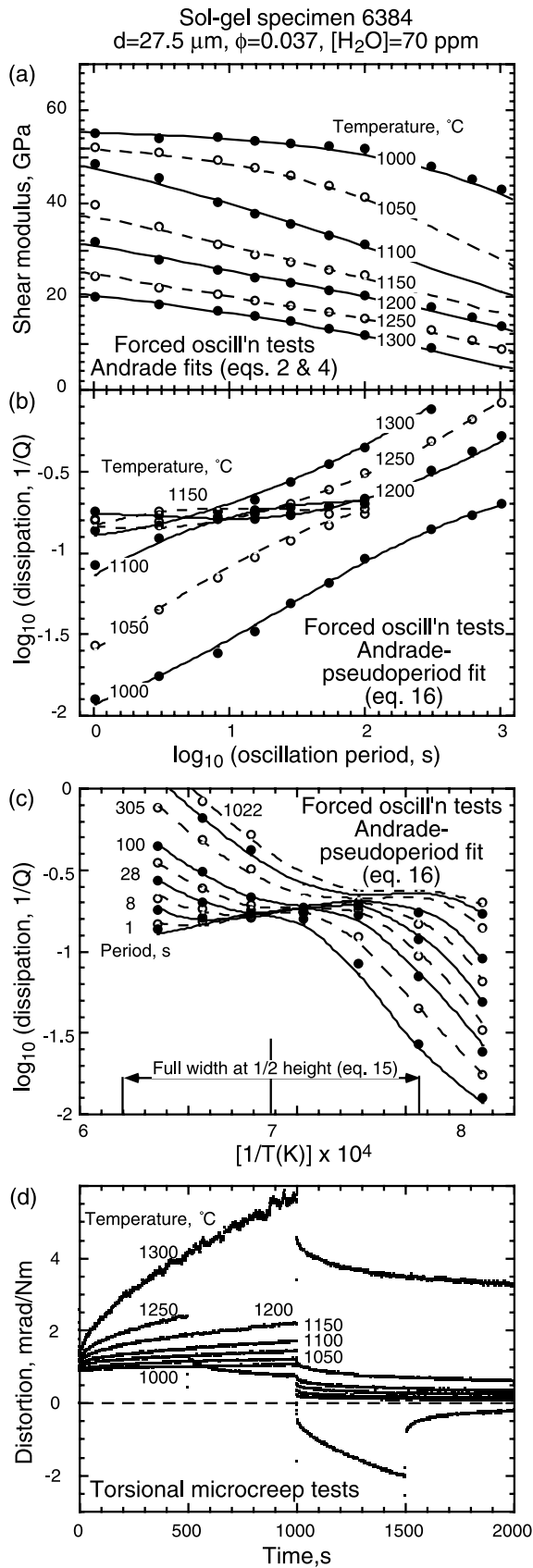


**Figure 4.** Results of mechanical testing of specimen 6384. Details as for Figure 2. The position of the peak center for 1 s period is indicated in Figure 4c along with the width at half height. See color version of this figure in the HTML.

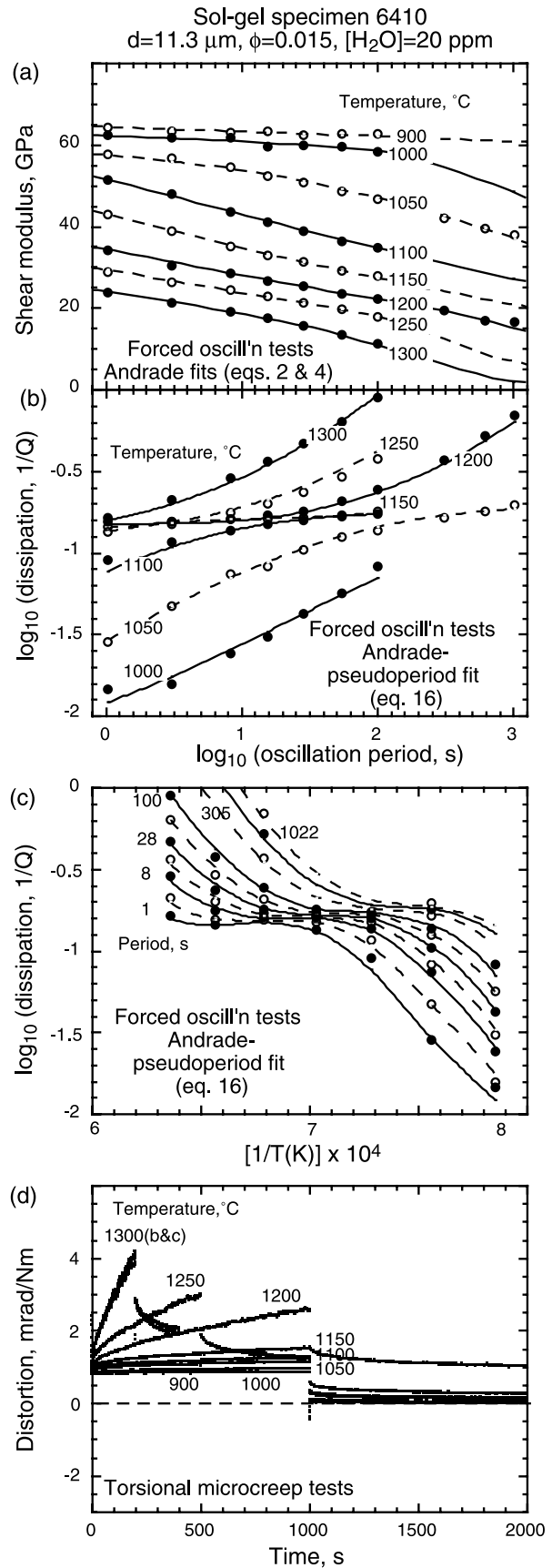


**Figure 5.** Results of mechanical testing of specimen 6410. Details as for Figure 2. See color version of this figure in the HTML.

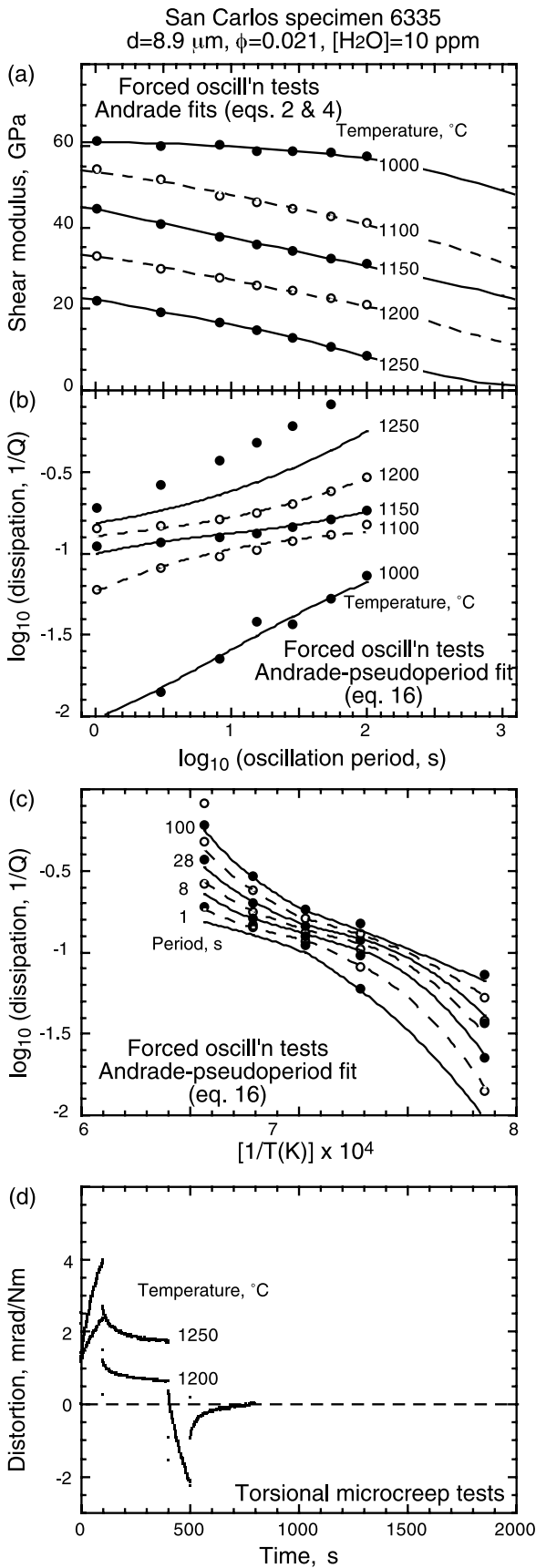


**Figure 6.** Results of mechanical testing of specimen 6335. Details as for Figure 2. See color version of this figure in the HTML.

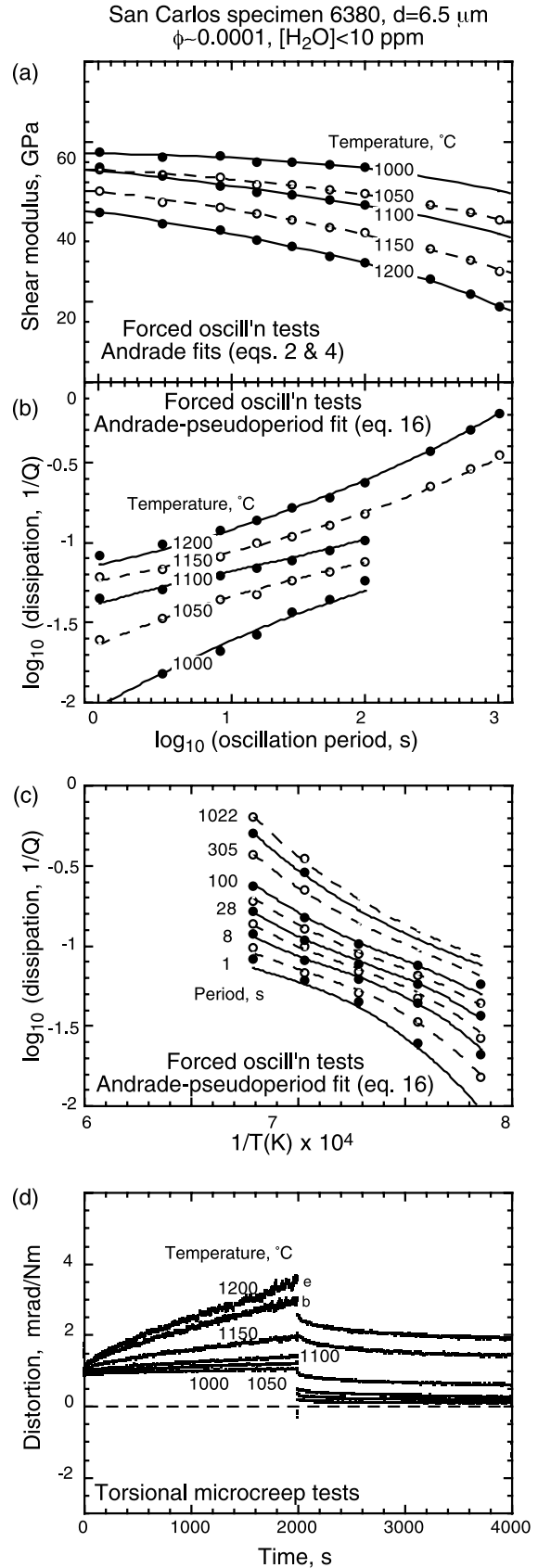


**Figure 7.** Results of mechanical testing of specimen 6380 [Jackson *et al.*, 2002] now known to contain a very small melt fraction  $\sim 0.0001$ . Details as for Figure 2. See color version of this figure in the HTML.

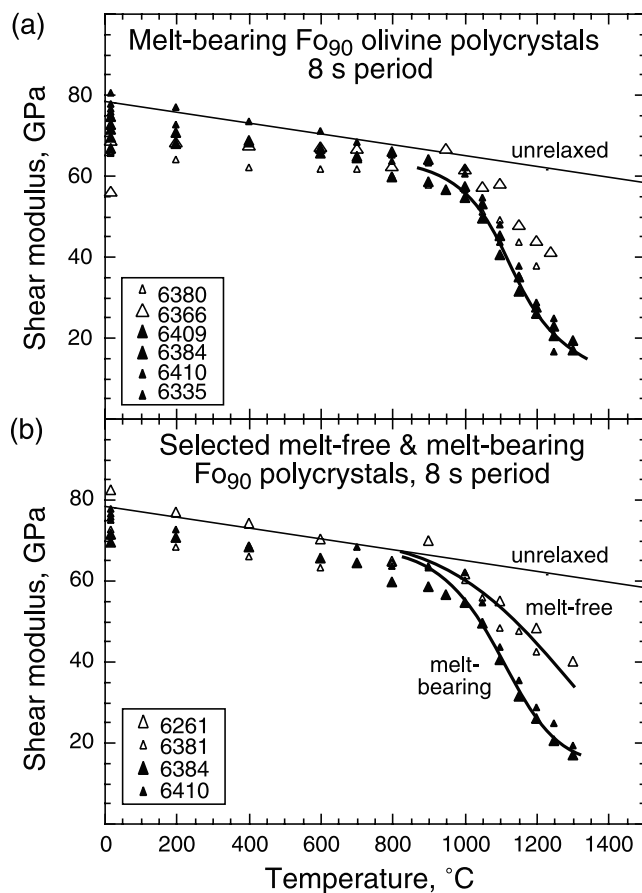


**Figure 8.** The temperature dependence of the shear modulus at the representative period of 8 s. (a) Data for all melt-bearing specimens of the present study, distinguished by different plotting symbols, are compared with the unrelaxed behavior calculated from high-frequency single-crystal elastic constants of *Isaak* [1992]. (b) A comparison of data for selected melt-bearing specimens with those for two representative melt-free olivine polycrystals from the studies of *Tan et al.* [2001] and *Jackson et al.* [2002]. See color version of this figure in the HTML.

dispersion (Figures 2a–7a). The systematic migration of the dissipation peak across the observational period range produces a subtle enhancement of the dispersion seen in local steepening of the  $G$  versus  $\log T_0$  trends at temperatures of 1050–1150°C in Figures 3a, 4a and 5a.

[23] For  $T > 900^\circ\text{C}$ , the  $G(T)$  trend for each of the melt-bearing specimens deviates markedly from the “unrelaxed” trend indicating strong viscoelastic relaxation of the shear modulus (Figure 8a). With the exception of specimens 6380 and 6366 (containing melt fractions of  $\sim 0.0001$  and 0.004, respectively, derived from minor impurities) the data indicate systematically stronger viscoelastic relaxation than for the melt-free specimens of comparable grain size (Figure 8b). As discussed by *Jackson et al.* [2002], the viscoelastic enhancement of  $|\partial G/\partial T|$  decreases with increasing grain size.

### 3.3. Microcreep Tests

[24] Microcreep tests were conducted and analyzed as previously described [*Jackson, 2000*], the standard protocol

involving 5 successive time intervals during which a steady torque of amplitude 0,  $+L$ , 0,  $-L$  and 0, respectively, was applied. In Figures 2d–7d the results are plotted, typically for the second and third segments of the record only. Records shorter than 2000 s total duration are plotted in their entirety. The parameters of Andrade fits to the modulus dispersion and dissipation inferred from frequency

**Table 2.** Andrade Fits to Processed Torsional Microcreep Records

Run Number (prior anneal, h)	$T$ , deg C	Duration, <sup>a</sup> s	$J_U$ , $10^{-1}$ GPa <sup>-1</sup>	$n^b$	$\beta$ , $10^{-2}$ GPa <sup>-1</sup> s <sup>-n</sup>	$\eta$ , $10^4$ GPa s	$\chi^2c$
<i>Specimen 6384</i>							
97813b(2 <sup>d</sup> )	1300	2500	.39(3)	.31(4)	3.0(3)	.09(2)	4.2
97813d <sup>e</sup> (6)		2500	.41(3)	.31(4)	2.9(3)	.09(2)	3.9
97813e <sup>f</sup> (22)		5000	.39(2)	.32(4)	2.2(2)	.19(6)	1.3
97813g(27)		2500	.40(3)	.32(4)	2.6(3)	.13(4)	2.2
978125a	1250	2500	.35(2)	.34(4)	1.5(2)	.46(25)	0.3
978125d		2500	.34(1)	.34(4)	1.5(2)	.42(21)	0.3
97812b	1200	5000	.29(1)	.34(3)	.88(8)	1.3(5)	0.6
978115b	1150	5000	.212(6)	.35(2)	.62(6)	3.3(21)	0.2
97811b	1100	5000	.177(4)	.35(3)	.40(4)	8.0(82)	0.1
978105b	1050	5000	.183(3)	.35(3)	.25(2)	7.4(51)	0.1
97810b	1000	5000	.183(2)	.38(4)	.10(1)	5.2(17)	0.3
<i>Specimen 6410</i>							
99413b <sup>f</sup> (3 <sup>d</sup> )	1300	1000	.29(3)	.31(5)	2.5(3)	.051(12)	1.0
99413c <sup>f</sup> (6)		1000	0.29(4)	.31(5)	2.8(4)	.045(10)	1.2
994125b <sup>f</sup>	1250	2500	.28(1)	.33(4)	1.4(1)	.25(8)	0.8
99412b	1200	5000	.244(9)	.33(3)	.92(9)	.63(14)	2.5
994115b	1150	5000	.199(4)	.35(3)	.46(4)	4.2(26)	0.2
99411b	1100	5000	.171(3)	.36(3)	.30(3)	19(37)	0.1
994105a	1050	5000	.166(2)	.36(3)	.20(2)	6.9(37)	0.2
99410b	1000	5000	.165(2)	.40(4)	.062(6)	6.2(19)	0.4
<i>Specimen 6409</i>							
99813b(2 <sup>d</sup> )	1300	1000	.34(2)	.32(4)	2.2(2)	.17(5)	1.7
99813d(4)		2500	.35(2)	.32(4)	2.2(2)	.16(5)	1.8
99813f <sup>f</sup> (6)		5000	.35(2)	.32(4)	2.0(2)	.18(5)	1.6
998125a <sup>f</sup>	1250	5000	.33(1)	.32(3)	.95(9)	1.0(3)	2.0
99812b <sup>f</sup>	1200	5000	.250(6)	.34(3)	.57(5)	2.6(13)	0.4
998115a	1150	5000	.192(4)	.35(3)	.40(4)	15(28)	0.2
99811a	1100	5000	.176(3)	.35(2)	.34(3)	(100)	0.7
998105a	1050	5000	.172(2)	.40(2)	.14(1)	(100)	2.0
99810a	1000	5000	.176(2)	.49(2)	.063(5)	(100)	8.1
<i>Specimen 6366</i>							
966124c(19 <sup>d</sup> )	1240	10000	.205(3)	.33(3)	.31(3)	4.4(20)	0.2
96612a	1200	10000	.195(3)	.34(3)	.22(2)	6.6(36)	0.1
96611a	1100	10000	.154(2)	.36(3)	.14(1)	141(970)	0.1
<i>Specimen 6335</i>							
910-14 <sup>g</sup> (2 <sup>d</sup> )	1250	1000	.26(5)	.29(6)	3.6(5)	.028(5)	2.6
910-12 <sup>h</sup> g	1200	1000	.28(2)	.33(5)	1.9(2)	.098(34)	0.1
<i>Specimen 6380<sup>h</sup></i>							

<sup>a</sup>Total duration of test comprising five equal time segments during which the applied torque successively assumes values of 0,  $L$ , 0,  $-L$ , and 0 respectively, unless indicated by <sup>f</sup>.

<sup>b</sup> $n \sim 1/3$  is a consequence of the procedure employed in fitting the raw time domain microcreep records [*Jackson, 2000*].

<sup>c</sup>Based on  $\sigma(G)/G = 0.03$  and  $\sigma(\log Q^{-1}) = 0.05$ .

<sup>d</sup>Numbers in parentheses after run numbers indicate the duration of prior annealing at the highest temperature in the indicated run. For specimen 6384 there was an additional 7.5 hours annealing at 1300°C prior to run 978.

<sup>e</sup>Halved torque amplitude.

<sup>f</sup>Fourth and fifth segments of record excluded from fit.

<sup>g</sup>Third and fifth segments of record three times longer than second and fourth segments.

<sup>h</sup>*Jackson et al.* [2002, Table 4].

**Table 3.** Fits to Temperature and Grain-Size Dependence of Viscosities Inferred From Microcreep Tests for Melt-Free and Melt-Bearing Specimens<sup>a</sup>

	$\eta_0$ , Pa s	$p$ , -	$E$ , kJ mol <sup>-1</sup>	Misfit, $(\chi^2/N)^{1/2}$
Melt-free	.60(365) $\times 10^2$	1.0(2)	298(71)	1.1
Melt-bearing	.74(535) $\times 10^{-6}$	2.2(3)	460(90)	1.9

<sup>a</sup>Equation (17) fitted to data of Figure 9 with specimen 6380 treated as melt-free (see text).

domain processing of the microcreep records are presented in Table 2.

[25] It is evident from Figures 2d to 7d that the creep rate increases systematically with increasing temperature and that the proportion of the creep strain recovered when the torque is removed decreases with increasing temperature – consistent with a progressively greater role for viscous deformation.

[26] The viscosities inferred from Andrade fits to the microcreep tests at temperatures of 1200–1300°C have been least squares fitted to equation (17) yielding the preferred values of  $\eta_0$ ,  $p$  and  $E$  presented in Table 3. The data are compared with the fit in Figure 9a. Notwithstanding its dissipation peak consistent with the presence of a small melt fraction ( $\sim 0.0001$ ), viscosities measured for specimen 6380 are clearly much more consistent with the trend for melt-free polycrystals (Figure 9b). Some of the scatter of the data about the optimal fit in Figure 9a to data for the remaining melt-bearing specimens is probably due to inter-specimen variation of melt fraction. Prior normalization (via equation 18) to the average melt fraction of 0.018 reduces the RMS misfit from 1.9 to 1.7 without significantly changing the values of the model parameters.

[27] The value of the grain-size exponent  $p = 2.2(3)$  is within the range (2–3) expected for diffusional creep [e.g., Hirth and Kohlstedt, 1995], unlike the corresponding value  $p = 1.0(2)$  for a more limited set of data for melt-free  $\text{Fo}_{90}$  olivine polycrystals (Figure 9b) and Jackson *et al.* [2002]. The microcreep tests on the melt-bearing materials sample the mechanical behavior further from the elastic threshold than those for the melt-free specimens so that viscous deformation plays a more dominant role. This provides a plausible explanation for the different grain-size sensitivities of the viscosity.

### 3.4. $Q^{-1}(T_0, T)$ Fits for the Individual Specimens

[28] In the first instance, the dissipation data measured for each melt-bearing specimen have been separately least squares fitted to equation (16) with pseudoperiods given by equations (5) and (10). This procedure, employing a non-linear Levenberg-Marquardt strategy [Press *et al.*, 1986], was repeated for various combinations of trial values of the activation energies  $E_B$  and  $E_P$  in order to minimize  $\chi^2$ . For the purpose of calculating  $\chi^2$  and the uncertainties in the model parameters, a uniform uncertainty of 0.05 log units in  $Q^{-1}$  was assumed.

[29] This approach provides an excellent representation of the dissipation data for specimens 6409, 6384, and 6410 – for each specimen fitting all data for the domain ( $1 < T_0 < 1022$  s and  $1000 < T < 1300^\circ\text{C}$ ) with an RMS misfit ( $\chi^2/N)^{1/2} < 1$  (Table 1). The smooth transition from nearly

frequency-independent behavior of  $Q^{-1}$  at 1150–1200°C to systematically stronger frequency dependence at both lower and higher temperatures is particularly well modelled (Figures 3b, 4b and 5b). The shape of the dissipation peak and its systematic displacement to shorter period with increasing temperature are more clearly seen in the plots of dissipation against reciprocal temperature in Figures 3c, 4c and 5c. Figure 4c includes an indication of the peak width at half height. The frequency and temperature dependence of  $Q^{-1}$  for specimen 6380 are similarly well reproduced by the Andrade-Gaussian-pseudoperiod model (Figures 7b and 7c). For specimen 6366 the combination of large grain size and small melt fraction results in lower levels of dissipation and accordingly more scatter about the optimal fit – particularly at 1000–1050°C (Figures 2b and 2c,

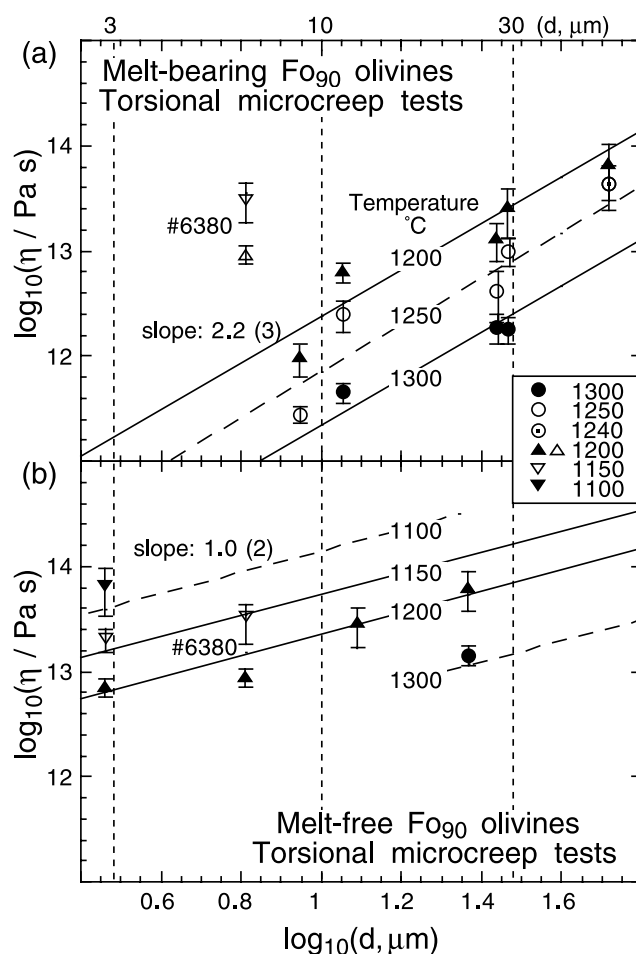


**Figure 9.** Grain-size and temperature sensitivity of viscosity  $\eta$  inferred from Andrade fits to the modulus dispersion and dissipation obtained by frequency domain processing of torsional microcreep records. The data are indicated by plotting symbols and the fits (Table 3) to equation (17) by the straight lines labeled with temperature in  $^\circ\text{C}$ . (a) Melt-bearing specimens of the present study. (b) Melt-free specimens [Jackson *et al.*, 2002]. As discussed in the text, the microcreep data for specimen 6380 (open triangles in (a)), notwithstanding its finite melt fraction ( $\sim 0.0001$ ), are better fitted by the  $\eta(d, T)$  trend for melt-free olivine polycrystals. See color version of this figure in the HTML.

Table 1). Specimen 6335 is more problematical: the dramatic increase in  $Q^{-1}$  between 1200 and 1250°C is not compatible with the behavior at lower temperatures that is adequately modelled (Figures 6b and 6c).

[30] It is noteworthy that no dissipation peak of significant height ( $>0.01$ ) was resolved when the same modeling strategy was applied to specimens 6261, 6365 and 6381 of our previous study [Jackson *et al.*, 2002].

### 3.5. Systematics Among Model Parameters for the Various Specimens

[31] The optimal values of the model parameters for these  $Q^{-1}(T_o, T)$  fits for each of the melt-bearing specimens are assembled in Table 1. The possibility that the peak height  $B$  and other parameters might assume significantly different optimal values associated with the different average melt fractions for the low- (1000–1150°C) and high- (1150–1300°C) temperature parts of the viscoelastic regime was also explored. However, it is evident from Table 1 that no such difference was resolved.

[32] The inter-specimen variability of the values of the model parameters of Table 1 may be summarized as follows: (1) The activation energies  $E_B$  for the dissipation background (350, 420, 510, 570, 580 and 610 kJ mol<sup>-1</sup>) are generally greater than for similar Andrade-pseudoperiod fits (see below) to data for the melt-free polycrystals 6381, 6365 and 6261 of Jackson *et al.* [2002]: 400, 460 and 470 kJ mol<sup>-1</sup>); (2) Even higher activation energies ( $E_P =$

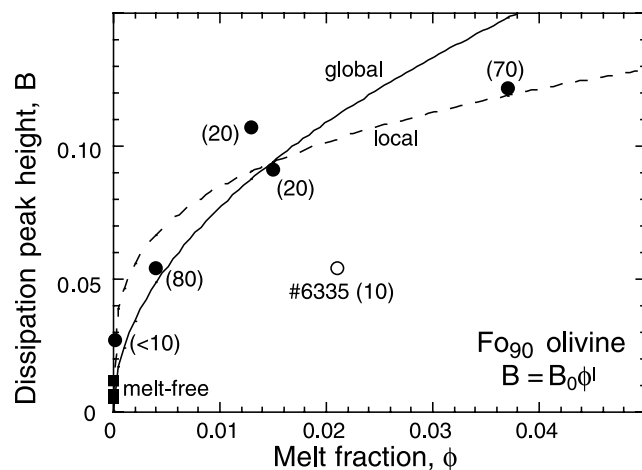


**Figure 10.** The variation of dissipation peak height  $B$  with maximum melt fraction  $\phi$ . The circular plotting symbols represent the dissipation peak heights inferred for the individual specimens from the fits of Table 1. The dashed curve labeled “local” is a linear least-squares fit of these ( $\phi$ ,  $B$ ) data for all specimens except the texturally immature #6335 (open circle) to equation (22) with  $(B_0, l) = (0.28, 0.26)$ . The ‘global’ curve gives the  $B(\phi)$  variation prescribed by the fit to the  $Q^{-1}(T_o, T, d, \varphi)$  data for all melt-bearing specimens except 6335:  $(B_0, l) = (0.77, 0.50)$  ( $N = 261$ , Table 4). The numbers in parentheses indicate  $[H_2O]$  content in wt ppm. The peak heights ( $\leq 0.01$ ) formally obtained by applying the same Andrade-Gaussian-pseudoperiod fitting strategy to data for the melt-free specimens 6381, 6365 and 6261 are represented by the square plotting symbols at  $\phi = 0$ .

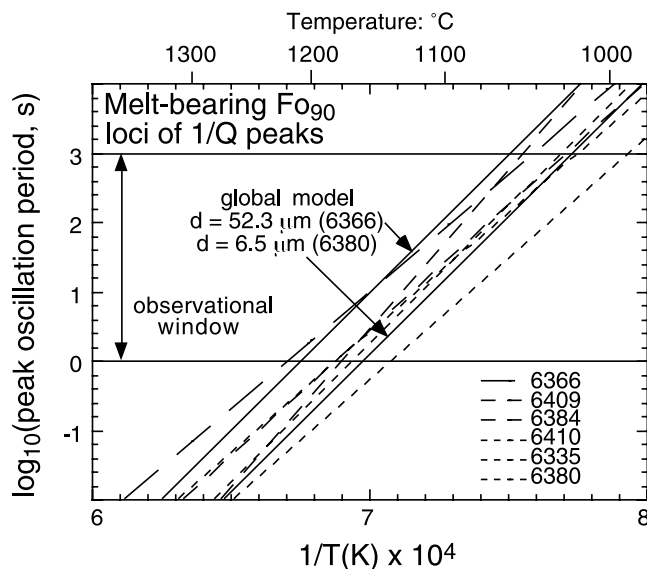


**Figure 11.** Loci of the centers of melt-related dissipation peaks in reciprocal absolute temperature – log period space. The fits to data for the individual specimens are plotted as broken lines whereas the pair of solid lines define the band occupied by the global Andrade-Gaussian-pseudoperiod  $Q^{-1}(T_o, T, d, \varphi)$  fit evaluated at the mean grain sizes of the individual specimens. In each case the slope of the line is  $E_P/R$  (see equations (12) and (21)). See color version of this figure in the HTML.

650–880 kJ mol<sup>-1</sup>) are needed to explain the strong temperature dependence of peak position (period). The difference between  $E_P$  and  $E_B$  generally decreases with decreasing grain size (from top to bottom of Table 1); (3) The grain-size sensitivity of the background is evident in the general tendency for the viscosity  $\eta$  to decrease with decreasing grain size down Table 1; however, no consistent trend is evident for  $\beta$ , the coefficient of the transient term in the Andrade creep function. (4) There is a clear positive correlation between peak height  $B$  and melt fraction  $\varphi$  (see also Figure 10) with specimen 6335 as an outlier. Generally similar values (2.4–3.3) of  $\sigma$  a measure of peak width, are observed for all six specimens. (5) The  $T-T_o$  loci of the dissipation peaks for the six specimens are relatively tightly clustered (Figure 11). During staged cooling, the center of the peak enters the observational window from periods shorter than 1 s at 1140–1220°C, moves steadily to longer periods with decreasing temperature, and finally leaves the observational window for periods longer than 1000 s at 990–1050°C. It is this very marked temperature sensitivity of the peak position that is reflected in the high activation energies  $E_P$ . The fact that  $\mu$ , the value of  $\ln X_P$  at the peak center, tends generally to decrease with decreasing grain size down Table 1 is evident in the ordering of the solid lines for the various specimens in Figure 11.

### 3.6. Parameterization of a Global Fit to the Dissipation Data: $Q^{-1}(T_o, T, d, \varphi)$

[33] The systematic inter-specimen variation of these model parameters suggests the possibility of a simultaneous fit to the data for all six specimens that includes not only the

**Table 4.** Global Fits to Dissipation  $Q^{-1}$  for Suites of Melt-Free and Melt-Bearing Fo<sub>90</sub> Specimens

Reference Parameters	Dissipation Background					Dissipation Peak					Misfit					
	$d_{\text{ref}}$ , $\mu\text{m}$	$T_{\text{ref}}$ , deg C	$m$	$E_{\text{B}}$ , kJ/mol	$J_U, 10^{-1}, \text{GPa}^{-1}$	$n$	$\beta, 10^{-2}, \text{s}^{-n} \text{GPa}^{-1}$	$\eta, 10^6, \text{GPa s}$	$E_{\text{P}}$ , kJ/mol	$B_0$	$l$	$\mu$	$\sigma$	$\chi^2$	N	$(\chi^2/N)^{1/2}$
Melt-free <sup>a</sup>	8.6	1100	1	390	(0.2)	.296(5)	.199(4)	.172(12)					384.1	131	1.71	
Melt-free <sup>b</sup>	8.6	1100	1	400	(0.2)	.283(6)	.195(5)	.193(16)					154.8	90	1.31	
Melt-bearing <sup>c</sup>	8.6	1100	1	540	(0.2)	.283(5)	.265(10)	.260(13)	750	.54(6)	.44(3)	2.87(11)	3.05(8)	899.4	296	1.74
Melt-bearing <sup>d</sup>	8.6	1100	1	520	(0.2)	.283(5)	.266(10)	.227(12)	720	.77(8)	.50(3)	2.73(9)	2.89(7)	478.5	261	1.35

<sup>a</sup>Data set of *Jackson et al.* [2002] for olivine polycrystals 6381, 6380, 6365 and 6261 augmented by 305–1022 s observations and fitted to the Andrade-pseudoperiod  $Q^{-1}(T_o, T, d)$  model based on equations (2) and (3) with pseudoperiod  $X_{\text{B}}$  specified by equation (19).

<sup>b</sup>As for footnote “a” but with specimen 6380 excluded.

<sup>c</sup>Fit of all data from present study and specimen 6380 to the Andrade-Gaussian-pseudoperiod model  $Q^{-1}(T_o, T, d, \varphi)$  of equation (16) with pseudoperiods  $X_{\text{B}}$  and  $X_{\text{P}}$  given by equations (19) and (20).

<sup>d</sup>Exclusion of data for the texturally immature specimen 6335 markedly reduces  $\chi^2$  without much change in the model parameters.

frequency and temperature dependence of  $Q^{-1}$  for each specimen but also the influence of both grain size and maximum melt fraction.

[34] An adequate global fit (Table 4) to the variation of  $Q^{-1}$  with frequency, temperature and grain size for the melt-free materials of *Jackson et al.* [2002] is obtained by incorporating grain-size ( $d$ ) sensitivity as follows into equation (5) for the background pseudoperiod  $X_{\text{B}}$ :

$$X_{\text{B}} = T_o(d/d_r)^{-m} \exp[(-E_{\text{B}}/R)(1/T - 1/T_r)]. \quad (19)$$

$d_r$  is an arbitrarily chosen reference grain size within the experimental range. Note that substitution of  $X_{\text{B}}$  given by equation (19) for  $T_o$  in equations (2) is equivalent to replacing a constant value of  $\beta$  by a grain-size and temperature-dependent analogue  $\beta (d/d_r)^{-nm} \exp[(-nE_{\text{B}}/R)(1/T - 1/T_r)]$  and  $\eta$  by an effective viscosity  $\eta (d/d_r)^m \exp[(E_{\text{B}}/R)(1/T - 1/T_r)]$ .

[35] Similarly use of

$$X_{\text{P}} = T_o(d/d_r)^{-m} \exp[(-E_{\text{P}}/R)(1/T - 1/T_r)] \quad (20)$$

in equations (9) and (8) confers grain-size sensitivity upon the peak position, the locus of which is now given by

$$\ln T_{\text{op}} = (E_{\text{P}}/R)(1/T_{\text{P}} - 1/T_r) + \mu + m \ln(d/d_r) \quad (21)$$

(c.f. equation (12)). In principle, different grain-size exponents  $m$  might have been anticipated for the background and peak pseudoperiods but, as explained below, it was found that a common value  $m = 1$  was adequate for modeling the results of the present study. The dependence of peak height  $B$  on melt fraction  $\varphi$  is modelled by a power law:

$$B = B_0\varphi^l \quad (22)$$

suggested by the trend shown in Figure 10. Thus  $B$  tends to zero as  $\varphi \rightarrow 0$  as required by the absence of a resolvable dissipation peak for our melt-free ( $\varphi < 0.0001$ ) specimens (Figures 1 and 10). Equations (16), (2, 3) and (8, 9 and 22) with the pseudoperiod master variables for background and peak given by equations (19) and (20) together constitute an Andrade-Gaussian-pseudoperiod model describing the variation of  $Q^{-1}$  for melt-bearing materials as a function of

frequency, temperature, mean grain size and maximum melt fraction, i.e.,  $Q^{-1} = Q^{-1}(T_o, T, d, \varphi)$ .

### 3.7. The Global Fit: $Q^{-1}(T_o, T, d, \varphi)$

[36] Regressions were performed with the parameters  $m$ ,  $E_{\text{B}}$  and  $E_{\text{P}}$  fixed at constant trial values during the simultaneous refinement of each of the other seven parameters  $n$ ,  $\beta$ ,  $\eta$ ,  $B_0$ ,  $l$ ,  $\mu$  and  $\sigma$ . This procedure was then repeated for other trial values of  $m$ ,  $E_{\text{B}}$  and  $E_{\text{P}}$  until the global minimum  $\chi^2$  was located (Table 4). No significant reduction in  $\chi^2$  results from allowing the value of the grain-size exponent  $m$  to vary from 1, in accord with our results for melt-free materials (Table 4). The implication, with the reasoning immediately following equation (19), is that a model with an effective viscosity  $\eta (d/d_r)^m \exp[(E_{\text{B}}/R)(1/T - 1/T_r)]$ , proportional to grain size  $d$  for  $m = 1$ , provides a satisfactory fit to the forced-oscillation  $Q^{-1}$  data. This result contrasts with the finding that the grain-size exponent  $p = 2.2(3)$  for the viscosities inferred from the microcreep tests (Figure 9a). The forced-oscillation data evidently sample mechanical behavior with a weaker grain-size sensitivity close to the threshold for elastic behavior [*Jackson et al.*, 2002]. It is presumably only at the longest oscillation periods ( $>100$  s) and in microcreep tests of relatively long duration that the viscous component of deformation with its stronger grain-size sensitivity becomes influential.

[37] The optimal  $m = 1$  fit (Table 4) is compared with all 296  $Q^{-1}$  data for the six melt-bearing specimens in Figure 12. The only data that are not reasonably well described by the model are the previously mentioned 1250°C data for 6335 which also deviate markedly from the  $Q^{-1}(T_o, T)$  fit for this specimen alone. With data for specimen 6335 excluded, the RMS misfit is 16% in  $Q^{-1}$ . This latter ( $N = 261$ ) model thus provides a satisfactory interim parameterization of the strain-energy dissipation for the melt-bearing olivine aggregates of the present study.

[38] The global fit is compared with data for the representative specimens 6384 and 6410 in Figures 13 and 14. Naturally, the global fit is inferior to those for the individual specimens plotted in Figures 2–7. For example, systematic deviations of the data from the global model (represented by the solid curves) are evident for specimen 6384 at 1200°C and for 6410 at 1300°C. Nevertheless, this simple model evidently provides an adequate overall fit to observed variation of  $Q^{-1}$  with frequency, temperature, grain size and melt fraction.

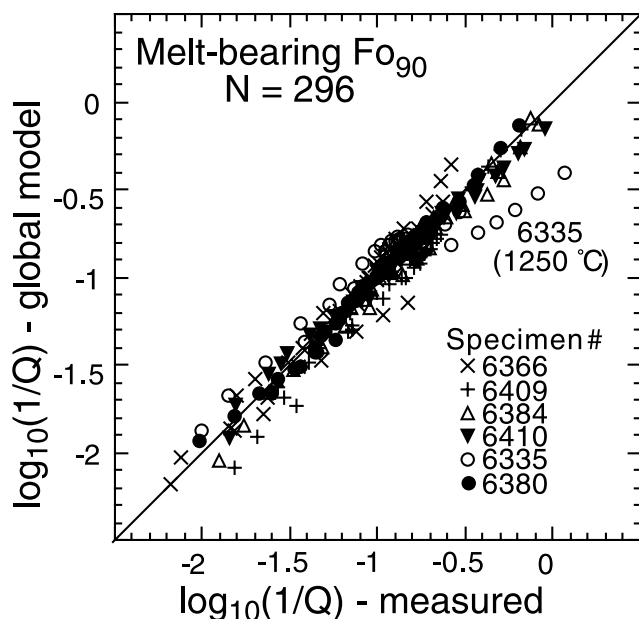


**Figure 12.** A comparison of measured and modeled dissipation for the melt-bearing specimens of the present study. The different plotting symbols denote the different specimens and the straight line represents a hypothetical perfect fit to the Andrade-Gaussian-pseudoperiod global  $Q^{-1}(T_o, T, d, \varphi)$  model. See color version of this figure in the HTML.

[39] Comparison of the curves for the global model with those for the background component (long-dashed curves) provides for ready visualization of the dissipation peak. For example, for specimen 6384 (Figure 13) it is evident that the peak is centered at a period of  $\sim 1000$  s at  $1000^\circ\text{C}$ , at  $\sim 10$  s period at  $1100^\circ\text{C}$  and at period  $< 1$  s at  $1200^\circ\text{C}$ . Thus the peak moves systematically across the observational window from long to short period with increasing temperature. As it does so, its superposition upon the usual monotonically frequency- and temperature-dependent background results in a major perturbation to the frequency dependence of attenuation. For 6384 at  $1000^\circ\text{C}$ , the short-period side of the dissipation peak contributes to stronger-than-normal frequency dependence, whereas at  $1150$ – $1200^\circ\text{C}$ , nearly frequency-independent behavior results from the superposition of background and the long-period side of the peak. By  $1300^\circ\text{C}$ , the influence of the dissipation peak is barely felt within the 1–1000 s observational window. Note that the melt-related dissipation peak for each specimen is adequately modelled as being of constant height and shape notwithstanding the changes in both melt fraction and composition resulting from progressive crystallization during staged cooling (documented in Part II).

[40] Also plotted for comparison in Figures 13 and 14 is the dissipation calculated from our Andrade-pseudoperiod

model for a melt-free olivine polycrystal of the same grain size. Evidently the background component of the global fit for the melt-bearing specimens and the model describing dissipation for melt-free materials are closely consistent at  $1000$ – $1050^\circ\text{C}$  but diverge progressively more widely with increasing temperature reflecting the stronger temperature sensitivity of the background in the melt-bearing materials ( $E_B = 520$  c.f.  $400$   $\text{kJ mol}^{-1}$  for the melt-free material, Table 4).

[41] Finally, a number of modeling issues remain for future investigation. As previously mentioned, it would be desirable to seek the distribution  $D(\tau)$  of anelastic relaxation times responsible for both the dissipation peak and the non-viscous part of the background. Incorporation of such a distribution  $D(\tau)$  into a Burgers creep function would allow the variations of both modulus and dissipation to be treated in an internally consistent manner. The covariance among the necessarily large number of model parameters should then also be closely examined. In constructing such a model, allowance should be made for the potentially different grain-size sensitivities of the anelastic and viscous behavior.

#### 4. Summary

[42] In preparation for the analysis and interpretation of Part II we review here the main features of the viscoelastic behavior for the suite of melt-bearing olivine polycrystals fabricated for and tested in this study. Of prime importance is the discovery of an essential qualitative difference between behavior of melt-bearing olivine polycrystals ( $\sim 0.0001 \leq \varphi \leq 0.037$ ) and that of melt-free materials of comparable grain size tested under similar conditions [Tan et al., 2001; Jackson et al., 2002]. The melt-bearing materials invariably display a broad strain energy dissipation peak superimposed upon an enhanced level of background dissipation.

[43] Remarkably consistent behavior is observed across a suite of six melt-bearing specimens despite differences in their origins and prior histories. The specimens were prepared from either San Carlos olivine (6366, 6409, 6335 and 6380) or sol-gel-derived  $\text{Fo}_{90}$  (6384, 6410) precursors. Basaltic melt was added to specimens 6409, 6384, 6410 and 6335. Small fractions of melt in 6366 and 6380 are due to minor impurities in the San Carlos olivine starting material. The cold-pressed pellets and the cylindrical specimens ground from the hot-pressed polycrystals were either oven-dried at  $\sim 100^\circ\text{C}$  (6335, 6366 and 6384) or pre-fired at  $1200^\circ\text{C}$  under controlled atmosphere (6409, 6410 and 6380). Residual bulk water contents [ $\text{H}_2\text{O}$ ] measured after mechanical testing range from  $< 10$  (6380) to 80 (6366) wt ppm  $\text{H}_2\text{O}$ . These varying amounts of water (retained mainly in the residual glass?) presumably reflect varying opportunities for the escape of water during hot-pressing and mechanical testing, and where appropriate, one-atmosphere

**Figure 13.** A comparison for specimen 6384 of measured dissipation (plotting symbols), the global  $Q^{-1}(T_o, T, d, \varphi)$  model ( $N = 261$ , Table 4, solid curve), the background part  $Q_B^{-1}(T_o, T, d)$  of the global model (long dashed curve), and the dissipation  $Q_B^{-1}(T_o, T, d)$  expected of melt-free material of the same grain size ( $N = 90$ , Table 4, short-dashed curve). The contribution of the melt-related dissipation peak is the difference between the global fit and its background component. See color version of this figure in the HTML.

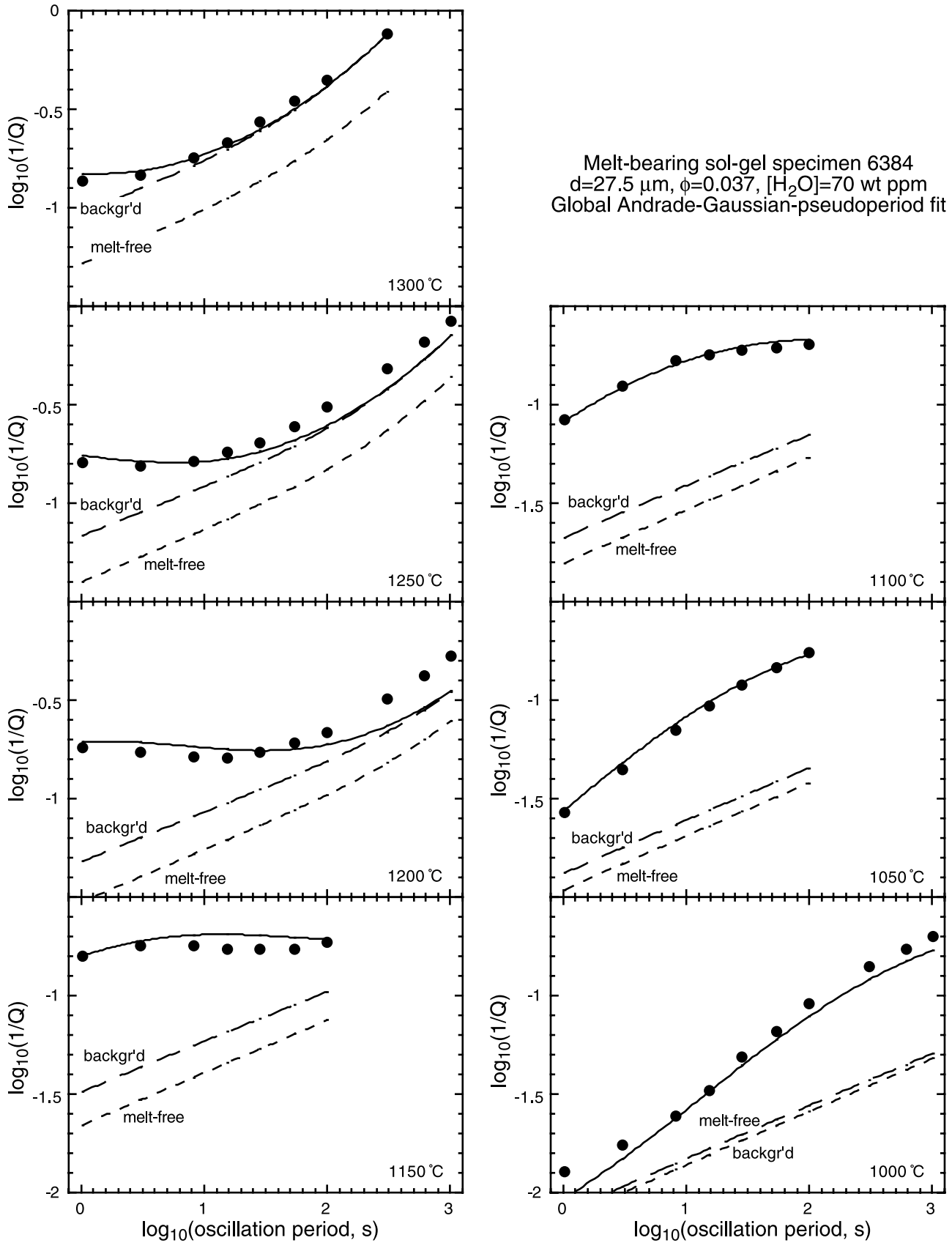


Figure 13

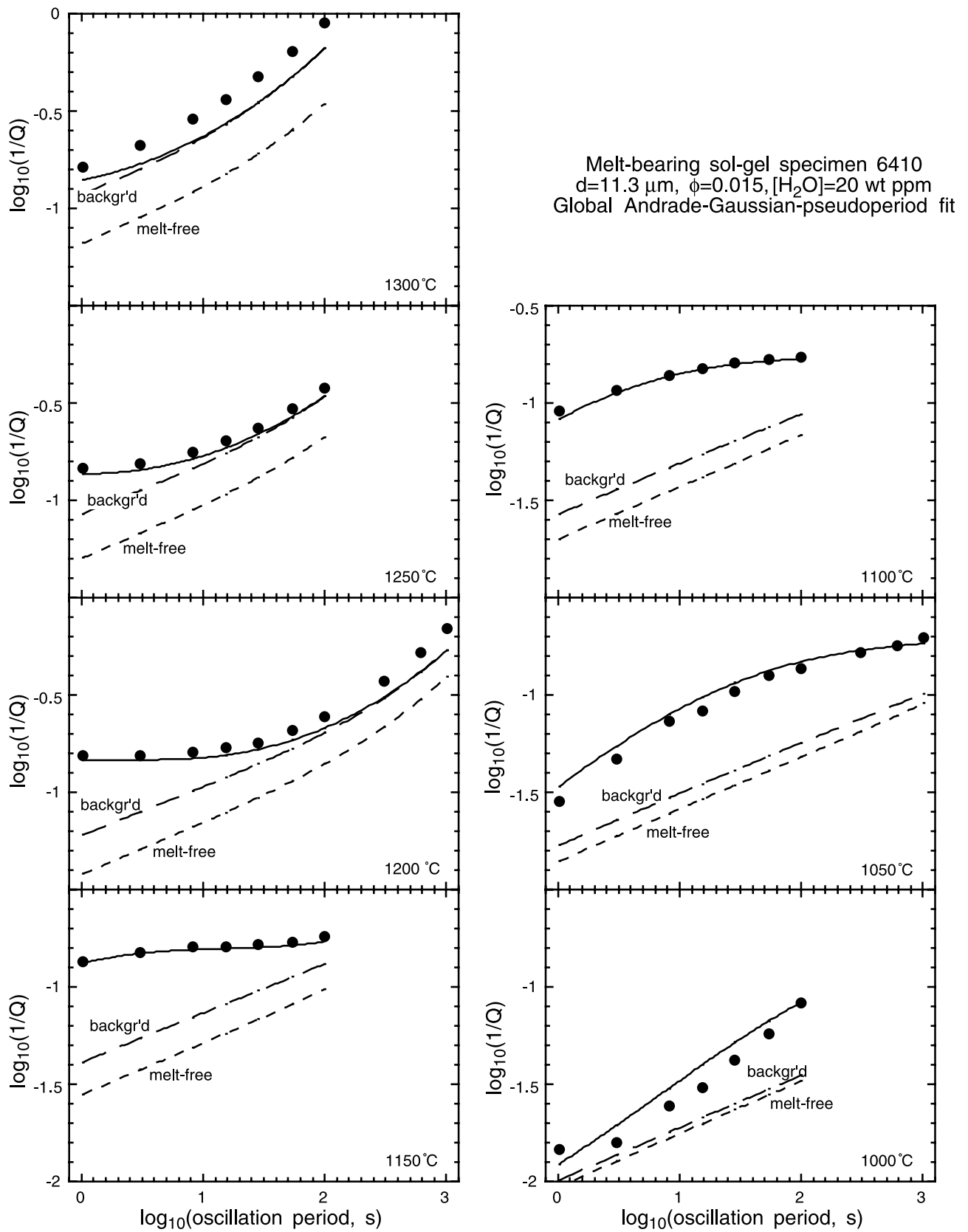


Figure 14. Specimen 6410. Details as for Figure 13. See color version of this figure in the HTML.

fining. No systematic variation of  $Q^{-1}$  with  $[H_2O]$  was observed in this study. However, a thorough investigation is deferred for future work. Specimens were hot-pressed and mechanically tested within mild steel sleeves lined internally with either Fe (6335) or Ni  $_{70}Fe_{30}$  foil - the latter intended to produce more oxidising conditions within the stability field of natural Ni-bearing olivine. Mean grain sizes range from 6.5 to 52.3  $\mu\text{m}$ , and melt fractions at maximum temperature from  $\sim 0.0001$  to 0.037.

[44] The high-temperature ( $T \geq 1000^\circ\text{C}$ ) dissipation data for each specimen are adequately described by a model involving a Gaussian peak of fixed height and shape superimposed upon a dissipation background that varies monotonically with oscillation period and temperature. For the most comprehensive data sets (for individual specimens 6409, 6384 and 6410 tested at temperatures of 1000–1300 $^\circ\text{C}$ ) the RMS misfit  $(\chi^2/N)^{1/2}$  of the measured dissipation is only 0.4 to 0.6. Separation of low- and high-temperature subsets produced no significant changes in the optimal values of the parameters  $B$ ,  $\mu$  and  $\sigma$  related to peak height, position and width, respectively (Table 1). Even at 1000 $^\circ\text{C}$  where crystallization of the melt is essentially complete (Part II), the presence of the peak is felt in the enhanced frequency dependence of  $Q^{-1}$  (especially clear in Figure 13). It follows that the peak height does not reflect the volume fraction of melt actually present at any given temperature since melt fraction changes markedly with progressive crystallization during staged cooling (Part II).

[45] The dissipation peak width (expressed as full width at half-height  $\delta \log T_0|_T$  – equation (14)) varies only mildly among the fits for the individual specimens from 2.4 log units for 6384 to 3.3 log units for 6380 (Table 1). With  $\delta \log T_0|_T = 2.9$  for the ( $N = 261$ ) global fit, the melt-related dissipation peak is much broader than the Debye peak ( $\delta \log T_0|_T = 1.1$ ) of the standard anelastic solid with its unique anelastic relaxation time. The clear implication is that the process responsible for the dissipation peak must have a distribution  $D(\tau)$  of anelastic relaxation times  $\sim 2$  log units wide [c.f. *Kampfmann and Berckhemer*, 1985].

[46] Another striking characteristic of the melt-related dissipation peak is the very high activation energy  $E_P$  required to model the strong temperature sensitivity of its position (period) (Figure 11). Optimal values of  $E_P$  for individual specimens vary from 650 to 880  $\text{kJ mol}^{-1}$ , with a preferred value of 720  $\text{kJ mol}^{-1}$  for the  $N = 261$  global model.

[47] The dissipation background for melt-bearing materials and  $Q^{-1}$  for melt-free materials of the same grain size display comparable frequency dependence and at 1000–1050 $^\circ\text{C}$  are essentially indistinguishable (Figures 13 and 14). However, the higher activation energy  $E_B$  for the melt-bearing background (520 compared with 400  $\text{kJ mol}^{-1}$ ) results in progressively greater divergence with increasing temperature between the melt-bearing background and the dissipation for the equivalent melt-free material. The melt-related enhancement of the background averages  $\sim 80\%$  at 1300 $^\circ\text{C}$ . The activation energy describing the temperature dependence of viscosity determined from the torsional microcreep records is similarly greater for the melt-bearing (460  $\text{kJ mol}^{-1}$ ) than for the melt-free (298  $\text{kJ mol}^{-1}$ ) materials.

## References

- Anderson, D. L., and C. G. Sammis (1970), Partial melting in the upper mantle, *Phys. Earth Planet. Inter.*, 3, 41–50.
- Berckhemer, H., W. Kampfmann, E. Aulbach, and H. Schmeling (1982), Shear modulus and  $Q$  of forsterite and dunite near partial melting from forced oscillation experiments, *Phys. Earth Planet. Inter.*, 29, 30–41.
- Cooper, R. F. (2003), Seismic wave attenuation: Energy dissipation in viscoelastic crystalline solids, in *Plastic Deformation in Minerals and Rocks*, *Rev. in Mineral. and Geochem.*, vol. 51, edited by S. Karato and H. Wenk, pp. 253–290, Mineral. Soc. of Am., Washington, D. C.
- Findley, W. N., J. S. Lai, and K. Onaran (1976), *Creep and Relaxation of Non-Linear Viscoelastic Materials*, 367 pp., North-Holland, New York.
- Forsyth, D. W. (1992), Geophysical constraints on mantle flow and melt generation beneath mid-ocean ridges, in *Mantle Flow and Melt Generation at Mid-Ocean Ridges*, edited by J. P. Morgan, D. K. Blackman, and J. M. Sinton, pp. 1–66, AGU, Washington, D. C.
- Frost, H. J., and M. F. Ashby (1982), *Deformation-Mechanism Maps: The Plasticity and Creep of Metals and Ceramics*, 166 pp., Pergamon Press, New York.
- Gribb, T. T., and R. F. Cooper (1998), Low-frequency shear attenuation in polycrystalline olivine: Grain boundary diffusion and the physical significance of the Andrade model for viscoelastic rheology, *J. Geophys. Res.*, 103, 27,267–27,279.
- Gribb, T. T., and R. F. Cooper (2000), The effect of an equilibrated melt phase on the shear creep and attenuation behaviour of polycrystalline olivine, *Geophys. Res. Lett.*, 27, 2341–2344.
- Hammond, W. C., and E. D. Humphreys (2000a), Upper mantle seismic wave attenuation: Effects of realistic partial melt distribution, *J. Geophys. Res.*, 105, 10,987–10,999.
- Hammond, W. C., and E. D. Humphreys (2000b), Upper mantle seismic wave velocity: Effects of realistic partial melt geometries, *J. Geophys. Res.*, 105, 10,975–10,986.
- Hirth, G., and D. L. Kohlstedt (1995), Experimental constraints on the dynamics of the partially molten upper mantle: Deformation in the diffusion creep regime, *J. Geophys. Res.*, 100, 1981–2001.
- Isaak, D. G. (1992), High-temperature elasticity of iron-bearing olivines, *J. Geophys. Res.*, 97, 1871–1885.
- Jackson, I. (2000), Laboratory measurement of seismic wave dispersion and attenuation: Recent progress, in *Earth's Deep Interior: Mineral Physics and Tomography From the Atomic to the Global Scale*, edited by S. Karato et al., pp. 265–289, AGU, Washington, D. C.
- Jackson, I., and M. S. Paterson (1993), A high-pressure, high temperature apparatus for studies of seismic wave dispersion and attenuation, *Pure Appl. Geophys.*, 141, 445–466.
- Jackson, I., U. H. Faul, J. D. Fitz Gerald, and B. H. Tan (2002), Grain-size sensitive seismic-wave attenuation in polycrystalline olivine, *J. Geophys. Res.*, 107(B12), 2360, doi:10.1029/2001JB001225.
- Kampfmann, W., and H. Berckhemer (1985), High temperature experiments on the elastic and anelastic behaviour of magmatic rocks, *Phys. Earth Planet. Inter.*, 40, 223–247.
- Mavko, G. M. (1980), Velocity and attenuation in partially molten rocks, *J. Geophys. Res.*, 85, 5173–5189.
- Mavko, G. M., and A. Nur (1975), Melt squirt in the asthenosphere, *J. Geophys. Res.*, 80, 1444–1448.
- Nowick, A. S., and B. S. Berry (1972), *Anelastic Relaxation in Crystalline Solids*, 677 pp., Academic, San Diego, Calif.
- O'Connell, R. J., and B. Budiansky (1977), Viscoelastic properties of fluid-saturated cracked solids, *J. Geophys. Res.*, 82, 5719–5735.
- Press, W. H., B. P. Flannery, S. A. Teukolsky, and W. T. Vetterling (1986), *Numerical Recipes: The Art of Scientific Computing*, 818 pp., Cambridge Univ. Press, New York.
- Sato, H., I. S. Sacks, T. Murase, G. Muncill, and H. Fukuyama (1989),  $Q_p$ -melting temperature relation in peridotite at high pressure and temperature: Attenuation mechanism and implications for the mechanical properties of the upper mantle, *J. Geophys. Res.*, 94, 10,647–10,661.
- Schmeling, H. (1985), Numerical models on the influence of partial melt on elastic, anelastic and electric properties of rocks. Part I: Elasticity and anelasticity, *Phys. Earth Planet. Inter.*, 41, 34–57.
- Shankland, T. J., R. J. O'Connell, and H. S. Waff (1981), Geophysical constraints on partial melt in the upper mantle, *Rev. Geophys. Space Phys.*, 19, 394–406.
- Tan, B. H., I. Jackson, and J. D. Fitz Gerald (1997), Shear wave dispersion and attenuation in fine-grained synthetic olivine aggregates: Preliminary results, *Geophys. Res. Lett.*, 24, 1055–1058.

- Tan, B. H., I. Jackson, and J. D. Fitz Gerald (2001), High-temperature viscoelasticity of fine-grained polycrystalline olivine, *Phys. Chem. Miner.*, *28*, 641–664.
- Walsh, J. B. (1968), Attenuation in partially melted material, *J. Geophys. Res.*, *73*, 2209–2216.
- Walsh, J. B. (1969), New analysis of attenuation in partially melted rock, *J. Geophys. Res.*, *74*, 4333–4337.
- Xu, Y., M. E. Zimmerman, and D. H. Kohlstedt (in press, 2004), Deformation behaviour of partially molten mantle rocks, in *MARGINS Theoretical and Experimental Earth Science Series*, vol. 1, *Rheology and Deformation of the Lithosphere at Continental Margins*, edited by G. Karner et al., Columbia Univ. Press, New York.
- 
- U. H. Faul, J. D. Fitz Gerald, I. Jackson, and B. H. Tan, Research School of Earth Sciences, Australian National University, Canberra ACT 0200, Australia. (ian.jackson@anu.edu.au)